ACS APPLIED MATERIALS & INTERFACES

Research Article

www.acsami.org

Preparation of MIL-53(Fe)-Reduced Graphene Oxide Nanocomposites by a Simple Self-Assembly Strategy for Increasing Interfacial Contact: Efficient Visible-Light Photocatalysts

Ruowen Liang, Lijuan Shen, Fenfen Jing, Na Qin, and Ling Wu*

State Key Laboratory of Photocatalysis on Energy and Environment, Fuzhou University, Fuzhou 350002, P. R. China

Supporting Information

ABSTRACT: In this work, MIL-53(Fe)-reduced graphene oxide (M53-RGO) nanocomposites have been successfully fabricated by a facile and efficient electrostatic self-assembly strategy for improving the interfacial contact between RGO and the MIL-53(Fe). Compared with D-M53-RGO (direct synthesis of MIL-53(Fe)-reduced graphene oxide nanocomposites via one-pot solvothermal approach), M53-RGO nanocomposites exhibit improved photocatalytic activity compared with the D-M53-RGO under identical experimental conditions. After 80 min of visible light illumination ($\lambda \geq 420$ nm), the reduction ratio of Cr(VI) is rapidly increased to 100%, which is also higher than that of reference sample (N-doped TiO_2). More significantly, the M53-RGO nanocomposites are proven to perform as bifunctional photocatalysts with considerable activity in the mixed systems (Cr(VI)/dyes) under visible light, which made it a potential candidate for industrial wastewater treatment. Combining with photoelectrochemical analyses, it could be revealed that the introduction of RGO would minimize the recombination of photogenerated electron−hole pairs. Additionally, the effective interfacial contact between MIL-53(Fe) and RGO surface would further accelerate the transfer of photogenerated electrons, leading to the enhancement of photocatalytic activity of M53-RGO toward photocatalytic reactions. Finally, a possible photocatalytic reaction mechanism is also investigated in detail.

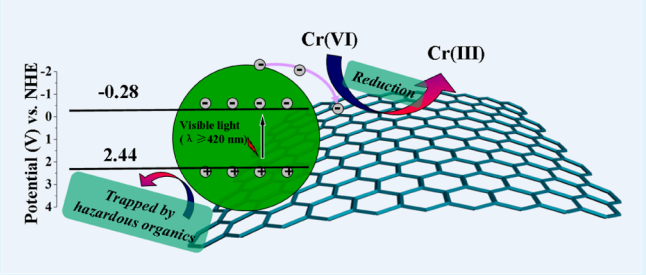

KEYWORDS: *MIL-53(Fe), graphene, self-assembly, photocatalysis, Cr(VI), dyes, visible light*

1. INTRODUCTION

Metal−organic frameworks (MOFs) are a new class of organic−inorganic hybrid solids and have been one of the fastest developing fields of chemistry.[1−3] Their unique properties such as structural flexibility and large specific surface area have led to the successful application of MOFs in magnetism, adsorption, sensor devices, drug release, and catalysis.[4−8] Especially, more and more attention has been paid to exploring the MOF materials as a new type of photocatalysts.[9−12] As a typical MOF material, Fe−benzenedicarboxylate (MIL-53(Fe)), built up by 1,4-bezenedicarboxylate (H_2BDC) linker and $FeO_4(OH)_2$ octahedra, is of special interest because of its potentials in gas storage, drug delivery, and lithium-ion battery.[13−16] Because of the small size of the Fe(III)−oxide cluster, limited recombination of the photogenerated charge carriers and thus a superior photoactivities could be expected in such MOFs. Recently, MIL-53(Fe) has been reported to exhibit considerable photocatalytic activity in the decolorization of organic dyes.[17] In our previous study, we have also demonstrated that the MIL-53(Fe) shown the potential applications in photocatalytic reduction reaction.[18] To further improve the photocatalytic performances of MOFs, some researchers have focused their efforts on the introduction of functional entities into such materials.[19,20] To date, the simply random integration of MOFs and functional entities has still been the most common synthesis route for MOF-based nanocomposites. However, this route typically results in irregular morphologies, a poor interfacial contact and low photocatalytic performance.[21,22] Therefore, it is of significance to develop a simple and direct approach to modify MOFs photocatalyst with hyper-efficient structures and fascinating properties.

Graphene, as a new type of carbon materials with unique 2D structure and high electron conductivity, has been projected as a rising star in the field of materials science.[23,24] More recently, graphene has also been regarded as an ideal building block for photocatalyst carrier and promoter.[25,26] Proper integration of MOFs with 2D graphene sheets with an appropriate strategy would further enhance photocatalytic performance of graphene oxide (RGO)-based nanocomposites for target reactions. To achieve efficient RGO-based photocatalysts, one should consider how to adequately harness the excellent electron conductivity and unique 2D structure and of RGO. Recent works have demonstrated that electrostatic self-assembly is an

Received: January 22, 2015
Accepted: April 20, 2015
Published: April 20, 2015

DOI: 10.1021/acsami.5b00682
ACS Appl. Mater. Interfaces 2015, 7, 9507−9515

ideal technique for constructing efficient RGO-based photocatalysts, by which the RGO sheets can cover with photocatalysts fully and intimately.[27,28] Because of the strong interfacial contact between RGO and photocatalysts, we can maximize the extraordinary electron-transport property of RGO, thereby leading to the enhancement of the MOFs' photocatalytic activity. Although there have been some reports on the interfacial contact between semiconductors and RGO,[29,30] the research works focused on investigating the interfacial contact between MOFs and RGO are rather scarce, especially, the relations with photocatalytic performance have not been studied so far.

In this paper, we primarily focus on the fabrication of MIL-53(Fe)-reduced graphene oxide (M53-RGO) nanocomposites and, specifically, their application in the environment restoration. M53-RGO is fabricated via an efficient electrostatic self-assembly method. That is, electrostatic assembly of negatively charged graphene oxide (GO) with positively charged MIL-53(Fe), followed by a solvothermal reduction of GO to RGO. By means of this approach, RGO sheets have a more intimate interfacial contact with MIL-53(Fe), which could lead to the more effective separation of photoexcited electron hole pairs than that of D-M53-RGO (direct synthesis of MIL-53(Fe)-reduced graphene oxide nanocomposites via one-pot solvothermal approach). This gives rise to the significantly enhanced the visible-light-driven photocatalytic performance of M53-RGO toward Cr(VI) reduction. More significantly, the M53-RGO nanocomposites are also proven to perform as bifunctional photocatalysts with considerable activity in the mixed systems (Cr(VI)/dyes) under visible light. Our work demonstrates the key role of interfacial contact between MOFs and RGO sheet, which affects the photocatalytic activities of MOF-RGO nanocomposites photocatalysts.

2. EXPERIMENTAL SECTION

2.1. Materials and Reagents. The following reagents and solvents were analytical grade and used as received from commercial suppliers without further purification. 1,4-benzenedicarboxylic acid (H_2BDC) and potassium dichromate ($K_2Cr_2O_7$) were obtained from Alfa Aesar China Co., Ltd.. Iron(III) chloride hexahydrate ($FeCl_3 \cdot 6H_2O$) was supplied by Aladdin Reagent Co., Ltd. Methanol (CH_4O), ethanol (C_2H_5OH), graphite powder, sulfuric acid (H_2SO_4, 70%), nitric acid (HNO_3, 65%), hydrochloric acid (HCl, 37%), ammonium oxalate (AO), potassium persulfate ($K_2S_2O_8$), phosphorus pentoxide (P_2O_5), N,N-dimethylformamide (DMF), hydrogen peroxide (H_2O_2, 30%), and potassium permanganate ($KMnO_4$) were supplied from Sinopharm Chemical Reagent Co., Ltd..

2.2. Preparation of Photocatalysts. *(a). Synthesis of MIL-53(Fe).* MIL-53(Fe) was synthesized according to the previous reports.[31,32] In a typical synthesis, a mixture of $FeCl_3 \cdot 6H_2O$, H_2BDC, and DMF (molar ratio = 1:1:280) was added into a Teflon liner under vigorous stirring for 60 min (1000 r min^{-1}). After that, Teflon liner was sealed in a stainless steel autoclave and heated at 170 °C for 24 h. The yellow MIL-53(Fe) powder was collected. To remove the guest molecules in the pores, the sample was stirred in methanol for 3 days. Then, the as-obtained yellow MIL-53(Fe) powder was filtered and dried under vacuum at 120 °C for 10 h.

(b). Synthesis of Graphene Oxide (GO). GO was synthesized according to our previous work.[33]

(c). Preparation of MIL-53(Fe)-reduced Graphene Oxide (M53-RGO) Nanocomposites via Electrostatic Self-Assembly Approach. 100 mg of MIL-53(Fe) was first dispersed in a certain amount of water. Then a negatively charged GO suspension in water with the desired weight addition was added into the above dispersion. After stirring for 60 min (500 r min^{-1}), the above MIL-53(Fe)-GO (M53-GO) suspension was centrifuged and washed with ethanol several times. Then the sediment was dispersed in 50 mL of ethanol and heated at 120 °C for 12 h. After the heat treatment, the obtained sample was washed with deionized water and dried at 60 °C. And the final products were labeled as M53-0.25% RGO, M53-0.5% RGO, M53-1% RGO, M53-3% RGO, M53-5% RGO, and M53-10% RGO.

(d). Direct Synthesis of MIL-53(Fe)-Reduced Graphene Oxide (D-M53-RGO) via One-Pot Solvothermal Approach. GO powder was dispersed in a certain volume of DMF by sonication for 120 min. Then a mixture of $FeCl_3 \cdot 6H_2O$ and H_2BDC (a molar ratio = 1:1) was dispersed in this suspension with vigorous stirring. After that, the Teflon liner was sealed in a stainless steel autoclave and heated at 170 °C for 24 h. Next, the obtained samples were cooled naturally to room temperature and washed with deionized water and dried at 60 °C. And then, a series of D-M53-RGO nanocomposites, including D-M53-0.25% RGO, D-M53-0.5% RGO, D-M53-1% RGO, D-M53-3% RGO, D-M53-5% RGO, and D-M53-10% RGO were obtained.

2.3. Characterizations. The zeta potentials (ξ) of the samples as a function of pH were determined by a Zetasizer 3000 instrument (Malvern Co., UK) at room temperature. Raman spectra were recorded on the Renishaw inVia Raman system 1000 with a 532 nm Nd: YAG excitation source. XRD patterns were carried on a Bruker D8 Advance X-ray diffrractometer operated at 40 kV and 40 mA with Ni-filtered Cu Ka irradiation (λ = 0.15406 nm). The data were recorded in the 2θ range of 5−50°. UV−vis diffuse reflectance spectra (UV−vis DRS) were obtained by a Cary 500 UV−vis−NIR spectrophotometer. Scanning electron microscopy (SEM) images were obtained on a Hitachi SU8000 scanning microscope at an accelerating voltage of 7 kV. Transmission electron microscopy (TEM) and high-resolution transmission electron microscopy (HRTEM) images were measured using a JEOL model JEM2010 EX microscope at an accelerating voltage of 200 kV. X-ray photoelectron spectroscopy (XPS) measurements were conducted on a PHI Quantum 2000 XPS system equipped with an Al X-ray source (1486.6 eV). The Mott−Schottky analysis and the electrochemical impedance spectroscopy (EIS) were performed at a Zahner electrochemical workstation. The photocurrent measurements were conducted on a Precision PARC workstation. The photoluminescence (PL) spectrum for samples were conducted on an Edinburgh FL/FS900 spectrophotometer. The time-resolved photoluminescence decay was investigated on an Edinburgh FLS 980 photoluminescence spectrometer (Edinburgh, UK). The concentration of Fe(III) in the suspension was detected by the Ultima2 ICP optical emission spectrometer. Furthermore, the mineralization degree of dye aqueous solutions was detected by total organic carbon (TOC) value, which was obtained by a Shimadzu TOC-VCPH analyzer.

2.4. Evaluation of Photocatalytic Activity. For the photocatalytic reduction of aqueous Cr(VI), an ozone-free 300 W Xe lamp (PLS-SXE 300, Trusttech Co. Ltd., Beijing) with 420 nm cut-off filter was used as the light source (420 nm $\leq \lambda \leq$ 760 nm). In the photocatalytic activity text, 40 mg of photocatalyst was suspended in 40 mL of 20 mg L^{-1} Cr(VI) aqueous solution. The pH value of reaction solution (pH 4) was adjusted with 2 mol L^{-1} H_2SO_4. After adding 5 mg of ammonium oxalate (hole scavenger), the suspension was stirred in the dark for 40 min to ensure the establishment of adsorption−desorption equilibrium. As the reaction proceeded, 4 mL of the sample solution was taken from the reactor at a scheduled interval and centrifuged. The concentration of Cr(VI) was determined colorimetrically at 540 nm using the diphenylcarbazide (DPC) method with a Cary 50 UV−vis spectrophotometer (Varian Co.).[34]

3. RESULTS AND DISCUSSION

To clarify the electrostatic self-assembly process, we have performed zeta potential (ξ) measurements. As displays in Figure 1, it can be observed that the isoelectric point of MIL-53(Fe) is at pH 7.1, indicating that the surface of MIL-53(Fe) is dominated by positively charges in neutral aqueous solution (ca. pH 6.0). As reported, the surface of GO colloids is negatively charged.[35,36] Therefore, the positively charged MIL-53(Fe) could integrate with the negatively charged GO by electrostatic interaction to form M53-RGO nanocomposites

DOI: 10.1021/acsami.5b00682
ACS Appl. Mater. Interfaces 2015, 7, 9507−9515

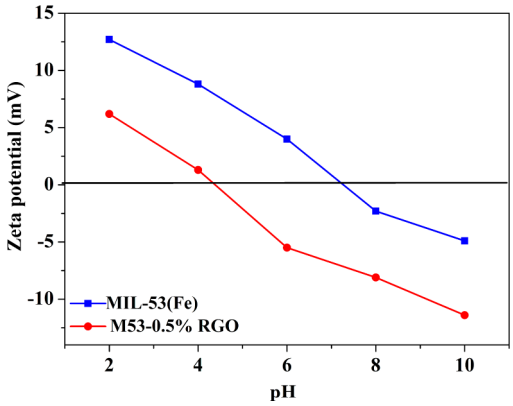

Figure 1. Zeta potential of MIL-53(Fe) and M53-0.5% RGO.

after the reduction of GO to RGO via a well-established solvothermal approach. In addition, when introduction of negatively charged GO into MIL-53(Fe), the zeta potential values are decreased gradually, which could be ascribed to the occurrence of the electrostatic attraction. To confirm the efficient reduction of GO to RGO after solvothermal reduction treatment, we have carried out Raman spectroscopy. The Raman spectra of original-GO and M53-RGO show the presence of D band (1350 cm^{-1}) and G band (1589 cm^{-1}) (see Figure S1 in the Supporting Information). The intensity ratio of D band and G band (I_D/I_G) is a measure of the relative concentration of the sp^3-hybridized defects compared to the sp^2-hybridized RGO domains.[37,38] The I_D/I_G value of original-GO is 1.04, suggesting the presence of high density of defects and structural disorder in original-GO. However, the I_D/I_G value of M53-RGO is decreased to 0.90, which indicates that more graphitization of the M53-RGO occurs after the solvothermal reduction treatment.

The XRD patterns of the as-prepared M53-RGO and D-M53-RGO nanocomposites are shown in Figure 2, respectively. It is obvious that all of the samples including MIL-53(Fe), M53-RGO, and D-M53-RGO exhibit similar XRD patterns, implying that the introduction of RGO has no effect on the crystal structure of MIL-53(Fe). Moreover, no characteristic diffractions for RGO can be observed in the M53-RGO nanocomposites, which could be ascribed to the low amount of RGO in the M53-RGO. Figure 3 shows the characteristic morphology of the original-MIL-53(Fe) and M53-RGO. As displayed in Figure 3A, the original-MIL-53(Fe) shows the block structure with the particle sizes of range from 8 to 15 μm.

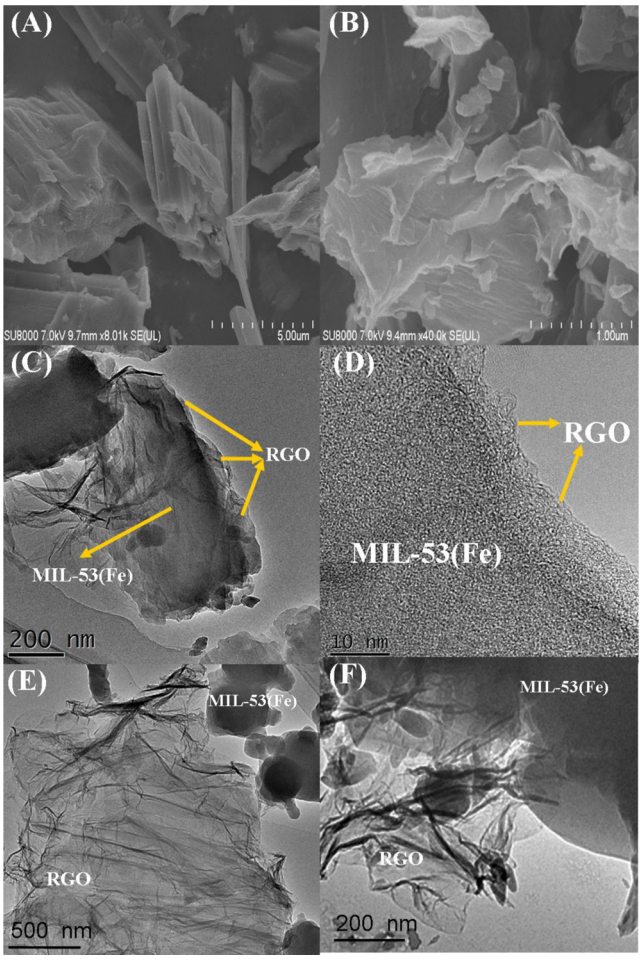

Figure 3. (A, B) SEM images of MIL-53(Fe) and M53-0.5% RGO, (C, D) TEM and HRTEM images of the M53-0.5% RGO, (E, F) TEM images of the D-M53-0.5% RGO.

The SEM image of obtained M53-RGO is displayed in Figure 3B. Apparently, the RGO and MIL-53(Fe) showing intimate interfacial contact, suggesting that such an efficient electrostatic self-assembly approach can make the two ingredients undergo a relatively adequate interfacial interaction. The TEM images of obtained M53-RGO are shown in Figure 3C, D, MIL-53(Fe) is wrapped by the curly RGO sheets, which leads to the surface of the particles being rougher. However, such an intimate interfacial contact of MIL-53(Fe) and RGO cannot be obtained

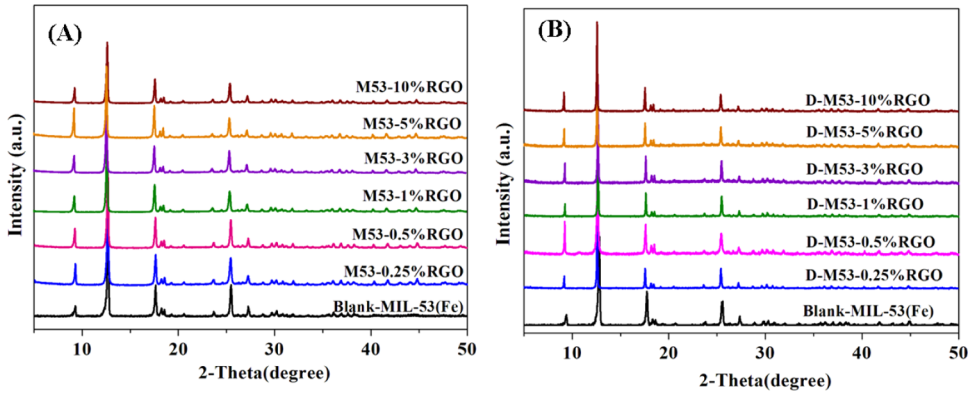

Figure 2. XRD pattens of (A) M53-RGO and (B) D-M53-RGO.

DOI: 10.1021/acsami.5b00682
ACS Appl. Mater. Interfaces 2015, 7, 9507−9515

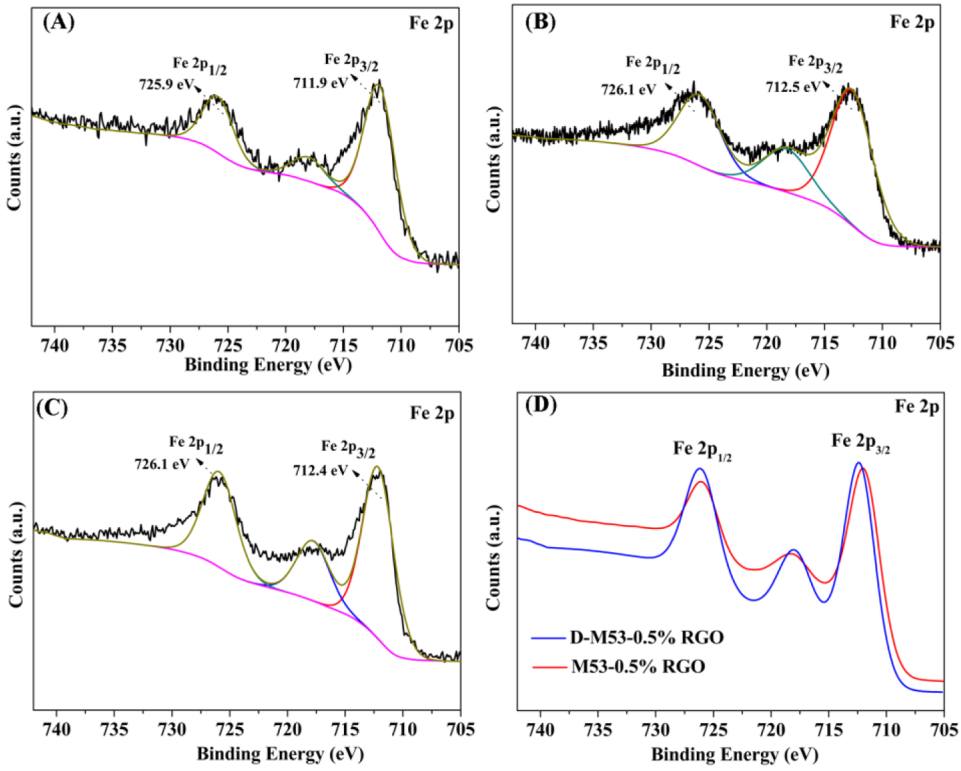

Figure 4. Fe 2p X-ray photoelectron spectroscopy (XPS) spectra of (A) M53-0.5% RGO, (B) MIL-53(Fe), (C) D-M53-0.5% RGO, and (D) comparison of the Fe 2p XPS spectra between M53-0.5% RGO and D-M53-0.5% RGO.

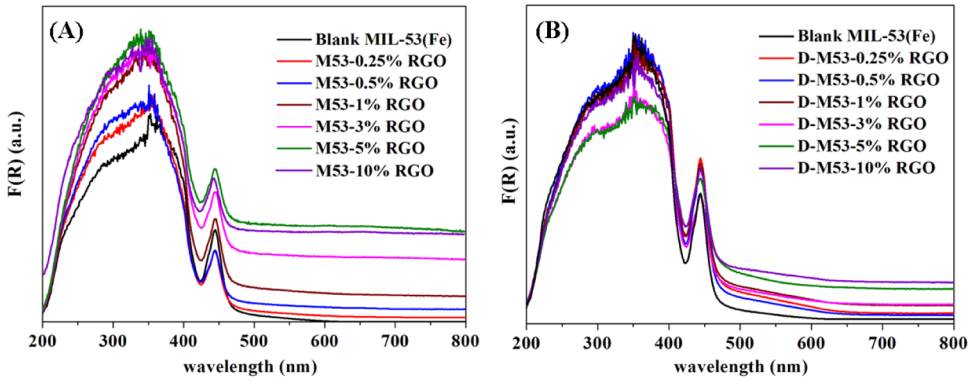

Figure 5. UV−vis diffuse reflectance spectra (UV−vis DRS) of (A) M53-RGO and (B) D-M53-RGO.

via the one-pot solvothermal approach. With the direct solvothermal method, MIL-53(Fe) and RGO integrate randomly, leading to the poor interfacial contact between MIL-53(Fe) and RGO sheet. The stacking RGO sheet is identified in the edge area of MIL-53(Fe), even some of the MIL-53(Fe) has no contact with RGO sheets (see Figure 3E, F). This is probably due to the surface charge of GO not being effectively utilized during the one-pot solvothermal process, because it would be restored to RGO before contact with MIL-53(Fe). Furthermore, as displayed in Figure S2 in the Supporting Information, there are even some black RGO sheets that can be observed in the suspension of D-M53-RGO. Thus, a simple integration of MIL-53(Fe) with RGO is not able to give a maximum interfacial contact between MIL-53(Fe) and RGO, which can be further confirmed from the X-ray photoelectron spectroscopy (XPS) results. Figure 4A shows the Fe 2p XPS spectrum of M53-0.5% RGO, two binding energy peaks at 711.9 eV (Fe $2p_{3/2}$) and 725.9 eV (Fe $2p_{1/2}$), corresponding to the Fe(III) (α-Fe_2O_3).[18] Furthermore, compared with the Fe(III) characteristic peaks of the MIL-53(Fe) (see Figure 4B) and D-M53-0.5% RGO (see Figure 4C), the XPS signature of the Fe 2p doublet for M53-0.5% RGO shifts to the lower binding energy (see Figure 4D). This can be ascribed to an intimate interfacial contact between RGO and MIL-53(Fe) in the M53-RGO nanocomposites.[39]

Figure 5 shows the UV−vis diffuse reflectance spectra (UV−vis DRS) of the as-obtained samples. With regard to all the samples, an intense UV absorption band appears at 244 nm is assigned to the ligand-to-metal charge transfer (LMCT), implying the bonding of carboxylate oxygen to metal.[40] Moreover, the small peak centered at 445 nm may be due to the transition ($^6A_{1g}$ => $^4A_{1g}$ + $^4Eg(G)$) in Fe(III).[41,42] In addiction, a red shift of the band gap transition is observed in all M53-RGO and D-M53-RGO nanocomposites. This

DOI: 10.1021/acsami.5b00682
ACS Appl. Mater. Interfaces 2015, 7, 9507−9515

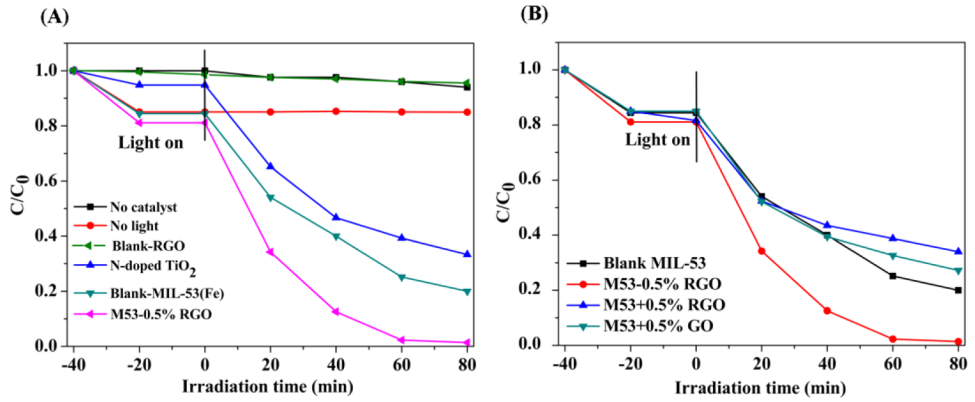

Figure 6. (A) Control experiments of photocatalytic reduction of Cr(VI) under different conditions and (B) comparison experiments of photocatalytic reduction of Cr(VI) under different conditions. Reaction conditions: 40 mg of photocatalyst, 40 mL of 20 mg L^{-1} Cr(VI), 5 mg of ammonium oxalate, air atmosphere, pH 4.

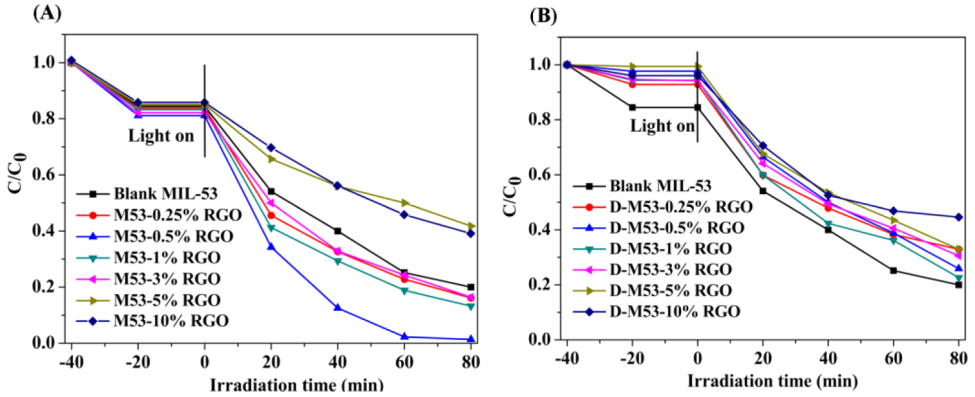

Figure 7. Photocatalytic reduction of aqueous Cr(VI) over (A) M53-RGO and (B) D-M53-RGO. Reaction conditions: 40 mg of photocatalyst, 40 mL of 20 mg L^{-1} Cr(VI), 5 mg of ammonium oxalate, air atmosphere, pH 4.

indicates that strong electronic interactions have been form between RGO sheets and MIL-53(Fe).[43−46] Notably, the increasing of RGO content in the M53-RGO nanocomposites (see Figure 5(A)) leads to a significant enhanced absorbance in the visible region range, which is consistent with the change of the M53-RGO nanocomposites from yellow to dark green. Moreover, the onset of the main optical absorption edge of M53-0.5% RGO is estimated to be 455 nm. Based on the relation $E_g = 1240/\lambda$, the calculated optical band gap of M53-0.5% RGO is 2.72 V. However, DRS spectra of D-M53-RGO are similar to that of original-MIL-53(Fe), implying that the introduction of RGO has a negligible effect on enhances the visible light absorption (see Figure 5(B)). It is further confirmed that electrostatic self-assembly approach is more effective than the one-pot solvothermal approach, which could lead to superior optical light absorption property.

To understand the advantages of electrostatic self-assembly approach on improving the photoactivity of M53-RGO nanocomposites, we have chosen Cr(VI) reduction as a model reaction. As can be seen from Figure 6A, the Cr(VI) could hardly be restored in the absence of photocatalyst or light. Moreover, it is obvious that a negligible reduction of Cr(VI) is observed in the present of blank-RGO. Instead, the reduction of Cr(VI) proceeds smoothly in the presence of photocatalyst. Importantly, M53-0.5% RGO also performs better than MIL-53(Fe) (79%) and N-doped TiO_2 (69%) under identical experimental conditions, respectively. After 80 min light irradiation ($\lambda \geq 420$ nm), the reduction ratio is ∼100%. Moreover, such photoactivity is higher than that of MIL-53(Fe)+0.5% RGO (67%) and MIL-53(Fe)+0.5% GO (72%), which are prepared by simply mixing MIL-53(Fe) and RGO (or GO) in proper proportions under identical conditions (see Figure 6(B)).

It is crucial to control the amount of RGO to achieve an optimal synergy interaction between RGO and MIL-53(Fe) for reduction of Cr(VI). As for M53-RGO nanocomposites (see Figure 7A), when a small amount of RGO is added (0.25%), the reduction ratio is rapidly increased to 81%. Moreover, when the content of RGO is increased to 0.5%, the highest photocatalytic activity is obtained. After 80 min of visible light illumination, almost 100% Cr(VI) can be restored. Nevertheless, when further increasing of RGO content, the photocatalytic activity gradual declines. The similar phenomenon has also been reported in other literatures.[47,48] For comparison purpose, photocatalytic performance of D-M53-RGO was also performed under identical conditions (see Figure 7B). Apparently, the D-M53-0.5% RGO displays a lower photoactivity than the sample of M53-0.5% RGO. However, it can be observed that, when the addition ratio of RGO is up to 5%, the photoactivity of M53-RGO is a little less than that of D-M53-RGO. Regarding the M53-RGO, the high content of RGO led to shield of the active sites on the MIL-53(Fe) surface and also rapidly decreased the photocatalytic performance.[49] For D-M53-RGO, the interfacial contact between RGO and MIL-53(Fe) in D-M53-RGO is very poor (see Figure S2 in the Supporting Information). There are still some pure MIL-

DOI: 10.1021/acsami.5b00682
ACS Appl. Mater. Interfaces 2015, 7, 9507−9515

53(Fe) that can absorb visible light directly and exhibit photoactivity. The difference changing tendency of photoactivity clearly implies that the electrostatic self-assembly is a superior approach for developing MOF-based nanocomposites.

The superiority of electrostatic self-assembly approach on enhancing the photocatalytic activity of M53-RGO nanocomposites can also be verified by the photocatalytic treatment of wastewater, which is also closely related to our daily life. In our present study, a mixed system is simulated using dye with natural pH (ca. 7) as the additional pollutant (20 mg·L^{-1}, no hole scavenger, air atmosphere). As for M53-0.5% RGO, after 300 min of visible light irradiation, the Cr(VI) reduction ratio is about 20.3%, the degradation ratios of MG, RhB are 22.2% and 43.0%, respectively, in the single systems (see Figure S3A in the Supporting Information). Notably, it is found that the combination of M53-0.5% RGO nanocomposite, Cr(VI), and organic dyes (MG or RhB) together can enable efficient Cr(VI) reduction and organic dyes oxidation under visible light irradiation. The enhanced photocatalytic activity of M53-0.5% RGO in the mixed systems might be ascribed to a synergistic effect between the photocatalytic redox processes. That is, photogenerated electrons and holes are captured by the Cr(VI) and dyes, respectively, which inhibits the recombination of photogenerated charge carriers. For comparison, photocatalytic activity of D-M53-0.5% RGO has been evaluated (see Figure S3B in the Supporting Information). As summarized in Table 1,

Table 1. Photocatalytic Activities of M53-0.5% RGO and D-M53-0.5% RGO in the Single/Mixed Systems[a]

samples	M53-0.5% RGO	D-M53-0.5% RGO	pollutants
Cr(VI) removal (%)	20.3	10.1	Cr(VI)
MG removal (%)	22.2	15.0	MG
RhB removal (%)	43.0	34.1	RhB
Cr(VI) removal (%)	70.4	33.3	Cr(VI)/MG
MG removal (%)	100.0	60.7	
Cr(VI) removal (%)	46.3	20.0	Cr(VI)/RhB
RhB removal (%)	83.1	40.4	

[a]Reaction conditions: 40 mg of photocatalyst, 40 mL of 20 mg L^{-1} Cr(VI)/dye, air atmosphere, pH 7.

the sample of M53-0.5% RGO exhibits much higher photocatalytic activity than that of D-M53-0.5% RGO in all experimental conditions, which made it a potential candidate for industrial wastewater treatment. Accordingly, it may be concluded that the interfacial contact plays a very important role in affecting the photocatalytic performance of MOF-based nanocomposites.

Additionally, the stability and reusability of M53-0.5% RGO have been investigated. In our work, photocatalyst was recovered by filtration, washed with 1 mol/L HNO_3 aqueous solution and water to completely remove the absorbed Cr(III) and dyes on the surface of M53-0.5% RGO. As shown in Figure S4A−C in the Supporting Information, photocatalytic activity of M53-0.5% RGO does not obviously decrease after four cycles, suggesting that the M53-0.5% RGO nanocomposite possesses high photostability. Furthermore, XRD and XPS results reveal that the crystal structure and surface chemical compositions of M53-0.5% RGO still keep unchanged even after the four cycles of the reaction (see Figure S4D, E in the Supporting Information). Moreover, the amount of Fe(III) ions leaching during the reaction has been quantified by ICP optical emission spectrometer (see Tables S1−S3 in the Supporting Information). It can be observed that there is almost no Fe(III) ions leaching from the M53-0.5% RGO during the reaction. Combining the above results, it can be concluded that the M53-0.5% RGO photocatalyst shows good catalytic reusability and stability in this reaction process. In addiction, the mineralization degree of dye aqueous solution has been detected. Figure S5−S7 in the Supporting Information present the typical time-course of TOC during irradiation in the presence of organic pollutants. Obviously, with the increase in irradiation time the TOC values are decreased significantly, which are consistent with the results of photocatalytic activity experiments.

To better understand the important role of sufficient interfacial contact between RGO and MIL-53(Fe) on promoting the lifetime of photogenerated electron−hole pairs and improving photoactivity, we have performed the photoelectrochemical experiments (see Figure 8A). Compared with other samples, M53-0.5% RGO prepared by the electrostatic self-assembly method exhibits the highest photocurrent density, suggesting a more efficient separation of the photoexcited electron−hole pairs. This can be further supported by the photoluminescence (PL) results. As shown in Figure 8B, for MIL-53(Fe), a broad band at 440−500 nm with a peak at 485 nm is detected, which is attributed to the 1,4-benzenedicarboxylic acid linkers in MIL-53(Fe) structure.[50] We can also found that the PL intensity of the photocatalyst followed the order: MIL-53(Fe) > D-M53-0.5% RGO > M53-0.5% RGO, indicating that the M53-0.5% RGO has the longest lifetime of electron−hole pairs. Furthermore, the room-temperature photoluminescence decay of M53-0.5% RGO exhibits a longer PL lifetime (∼77.6 ns) than the D-M53-0.5% RGO (∼76.1 ns) and MIL-53(Fe) (∼73.3 ns) (see Figure S8 and Table S4 in the Supportign Information), respectively. This long-lived charge-separated state makes the M53-0.5% RGO more efficient for photocatalytic applications. To further clarify the advantage of intimate interfacial contact in improving the charge carrier transfer, we have performed the electrochemical impedance spectra (EIS) Nyquist plot. As shown in Figure 8C, the M53-0.5% RGO has the smallest radius of curvature as compared to other samples, indicating the most efficient charge separation over M53-0.5% RGO nanocomposite, which confirms that interfacial contact indeed plays an important role in the improvement of photocatalytic performance.

To better clarify the electronic properties of M53-0.5% RGO, Mott−Sckottky measurements have been carried out. As displayed in Figure 9, the flat-band potential of M53-0.5% RGO is ca. −0.48 V vs Ag/AgCl at pH 6.8, corresponding to ca. −0.28 V vs NHE at pH 6.8, which is more negative than the Cr(VI)/Cr(III) potential (+0.51 V vs NHE).[51−53] Therefore, it is thermodynamically permissible for the transformation of photogenerated electrons to the Cr(VI) to produce Cr(III). Combining with the band gap energy estimated from UV−vis DRS spectra, valence band (VB) of M53-0.5% RGO is calculated to be 2.44 V vs NHE at pH 6.8, according to the empirical formula: $E_{CB} = E_{VB} - E_g$. As illustrated in the inset of Figure 9, in the mixed system, the VB level of M53-0.5% RGO is very close to the ·OH/OH^- potential (2.38 V vs NHE). Therefore, M53-0.5% RGO is not easy to oxidize OH^- to ·OH radicals under visible light irradiation. Notably, the redox potential of RhB and MG are about 1.43 and 0.90 V vs NHE, respectively,[54−56] which is more negative than the VB value of MIL-53(Fe), suggesting the direct hole oxidation pathway is available. Furthermore, active species trapping experiments

DOI: 10.1021/acsami.5b00682
ACS Appl. Mater. Interfaces 2015, 7, 9507−9515

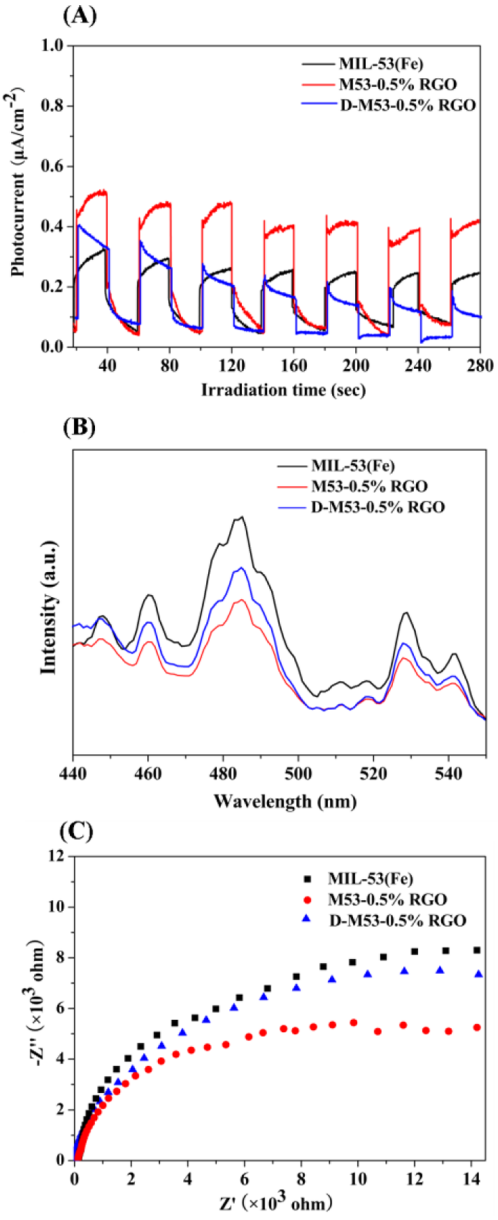

Figure 8. (A) Transient photocurrent response, (B) photoluminescence spectra, (C) Nyquist impedance plots of M53-0.5% RGO, D-M53-0.5% RGO, and MIL-53(Fe).

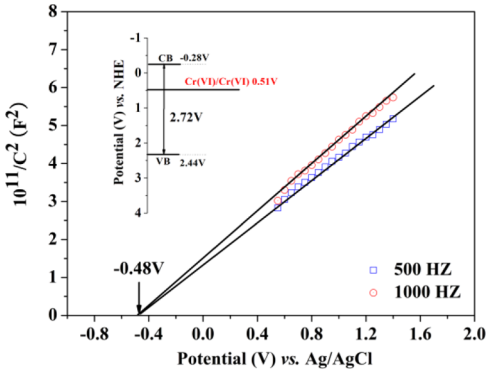

Figure 9. Typical Mott–Schottky plots of M53-0.5% RGO in 0.2 M Na_2SO_4 aqueous solution (pH 6.8).

using ammonium oxalate (AO) as quencher for photogenerated holes have further confirmed that the photocatalytic degradation process is driven by the photogenerated holes (see Table S5 in the Supporting Information).

Accordingly, a possible mechanism for the photocatalytic reduction of Cr(VI) and oxidation of hazardous organics over M53-RGO is proposed (see Figure 10). Under visible-light

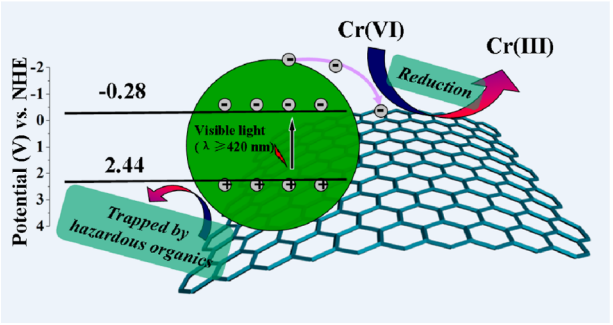

Figure 10. A schematic illustration of photocatalytic reduction Cr(VI) and oxidation of hazardous organics over M53-0.5% RGO under visible-light irradiation.

irradiation, M53-RGO is excited and photogenerated electrons/holes are generated. The photogenerated holes with strong oxidation capacity can oxidize the hazardous organics directly. Simultaneously, the photogenerated electrons can reduce Cr(VI) to Cr(III). Owing to the presence of RGO sheets, the photogenerated electrons are captured by the RGO, which inhibits the recombination of photogenerated electron–hole pairs efficiently. Furthermore, the unique 2D structure of RGO sheets allow the photocatalytic reactions to take place both on the surface of MIL-53(Fe) and RGO sheets, which increases the reaction centers and offers more catalytic sites. As a result, M53-RGO nanocomposites show great photocatalytic activities in photocatalytic redox reactions.

CONCLUSIONS

In summary, a series of MIL-53(Fe)-RGO (M53-RGO) nanocomposites have been successfully fabricated via an efficient electrostatic self-assembly method. That is, electrostatic assembly of negatively charged graphene oxide (GO) with positively charged MIL-53(Fe), followed by a solvothermal reduction of GO to RGO. The resulting M53-RGO photocatalysts exhibit improved activity compared with the D-M53-RGO toward the photoreduction of Cr(VI). And the optimal RGO content is found to be 0.5%, giving a corresponding Cr(VI) reduction ratio is 100% after 80 min of visible light irradiation. Further experiments reveal that electrostatic self-assembly approach could lead to a sufficient interfacial contact between MIL-53(Fe) and RGO sheets. Therefore, the lifetime of photogenerated charge carriers could be improved much more effectively as compared to the simply random integration of RGO and MIL-53(Fe) via one-pot solvothermal method. More significantly, M53-RGO nanocomposites also exhibit considerable photocatalytic activity in the mixed systems (Cr(VI)/dyes), which made it a potential candidate for industrial wastewater treatment. After 5 h of visible light illumination, the reduction ratio of Cr(VI) and the degradation ratio of dyes have been exceed 40 and 80%, respectively. It is hoped that our work could not only demonstrate the key role of adequate interfacial contact for

DOI: 10.1021/acsami.5b00682
ACS Appl. Mater. Interfaces 2015, 7, 9507–9515

improving photocatalytic performance, but also offer useful information on the fabrication of more efficient MOF-RGO photocatalysts toward specific applications.

■ ASSOCIATED CONTENT

Supporting Information

Raman spectra of original-GO and M53-0.5% RGO; photograph of M53-RGO and D-M53-RGO; photocatalytic activities of M53-0.5% RGO and D-M53-0.5% RGO in the mixed systems (Cr(VI)/dyes); reuse of M53-0.5% RGO for four successive cycles in the mixed systems (Cr(VI)/dyes); XRD patterns and XPS spectra of M53-0.5% RGO before and after the catalytic reaction; the concentration of Fe(III) during the reaction; time-course of TOC during irradiation; the photoluminescent (PL) lifetime of the samples; the results of active species trapping experiments. This material is available free of charge via the Internet at http://pubs.acs.org.

■ AUTHOR INFORMATION

Corresponding Author

*E-mail: wuling@fzu.edu.cn. Phone: +86-591-83779362. Fax: +86-591-83779105.

Notes

The authors declare no competing financial interest.

■ ACKNOWLEDGMENTS

This work was supported by the National Natural Science Foundation of China (21273036 and 21177024) and Science & Technology Plan Project of Fujian Province (2014Y2003).

■ REFERENCES

(1) Zhou, H. C.; Long, J. R.; Yaghi, O. M. Introduction to Metal−Organic Frameworks. *Chem. Rev.* **2012**, *112*, 673−674.

(2) Shen, L.; Liang, S.; Wu, W.; Liang, R.; Wu, L. Multifunctional NH_2-mediated Zirconium Metal−Organic Framework as an Efficient Visible-Light-Driven Photocatalyst for Selective Oxidation of Alcohols and Reduction of Aqueous Cr(VI). *Dalton Trans.* **2013**, *42*, 13649−13657.

(3) Gascon, J.; Hernandez-Alonso, M. D.; Almeida, A. R.; van Klink, G. P.; Kapteijn, F.; Mul, G. Isoreticular MOFs as Efficient Photocatalysts with Tunable Band Gap: an Operando FTIR Study of The Photoinduced Oxidation of Propylene. *ChemSusChem* **2008**, *1*, 981−983.

(4) Millward, A. R.; Yaghi, O. M. Metal−Organic Frameworks with Exceptionally High Capacity for Storage of Carbon Dioxide at Room Temperature. *J. Am. Chem. Soc.* **2005**, *127*, 17998−17999.

(5) Harbuzaru, B. V.; Corma, A.; Rey, F.; Atienzar, P.; Jordá, J. L.; García, H.; Ananias, D.; Carlos, L. D.; Rocha, J. Metal−Organic Nanoporous Structures with Anisotropic Photoluminescence and Magnetic Properties and Their Use as Sensors. *Angew. Chem., Int. Ed. Engl.* **2008**, *47*, 1080−1083.

(6) Vallet-Regi, M.; Balas, F.; Arcos, D. Mesoporous Materials for Drug Delivery. *Angew. Chem., Int. Ed.* **2007**, *46*, 7548−7558.

(7) Janiak, C. Engineering Coordination Polymers towards Applications. *Dalton Trans.* **2003**, 2781−2804.

(8) Farrusseng, D.; Aguado, S.; Pinel, C. Metal−Organic Frameworks: Opportunities for Catalysis. *Angew. Chem., Int. Ed. Engl.* **2009**, *48*, 7502−7013.

(9) Llabrés i Xamena, F. X.; Corma, A.; Garcia, H. Applications for Metal−Organic Frameworks (MOFs) as Quantum Dot Semiconductors. *J. Phys. Chem. C* **2006**, *111*, 80−85.

(10) Liang, R.; Shen, L.; Jing, F.; Wu, W.; Qin, N.; Lin, R.; Wu, L. NH_2-Mediated Indium Metal−Organic Framework as a Novel Visible-Light-Driven Photocatalyst for Reduction of the Aqueous Cr(VI). *Appl. Catal. B: Environ.* **2015**, *162*, 245−251.

(11) Shen, L.; Liang, S.; Wu, W.; Liang, R.; Wu, L. CdS-decorated UiO-66(NH_2) Nanocomposites Fabricated by a Facile Photodeposition Process: an Efficient and Stable Visible-Light-Driven Photocatalyst for Selective Oxidation of Alcohols. *J. Mater. Chem. A* **2013**, *1*, 11473−11482.

(12) Shen, L.; Wu, W.; Liang, R.; Lin, R.; Wu, L. Highly Dispersed Palladium Nanoparticles Anchored on UiO-66(NH_2) Metal−Organic Framework as a Reusable and Dual Functional Visible-Light-Driven Photocatalyst. *Nanoscale* **2013**, *5*, 9374−9382.

(13) Millange, F.; Guillou, N.; Medina, M. E.; Férey, G.; Carlin-Sinclair, A.; Golden, K. M.; Walton, R. I. Selective Sorption of Organic Molecules by the Flexible Porous Hybrid Metal−Organic Framework MIL-53(Fe) Controlled by Various Host−Guest Interactions. *Chem. Mater.* **2010**, *22*, 4237−4245.

(14) Taylor-Pashow, K. M. L.; Rocca, J. D.; Xie, Z.; Tran, S.; Lin, W. Postsynthetic Modifications of Iron−Carboxylate Nanoscale Metal−Organic Frameworks for Imaging and Drug Delivery. *J. Am. Chem. Soc.* **2009**, *131*, 14261−14263.

(15) de Combarieu, G.; Morcrette, M.; Millange, F.; Guillou, N.; Cabana, J.; Grey, C. P.; Margiolaki, I.; Férey, G.; Tarascon, J. M. Influence of the Benzoquinone Sorption on the Structure and Electrochemical Performance of the MIL-53(Fe) Hybrid Porous Material in a Lithium-Ion Battery. *Chem. Mater.* **2009**, *21*, 1602−1611.

(16) Liu, Y.; Her, J. H.; Dailly, A.; Ramirez-Cuesta, A. J.; Neumann, D. A.; Brown, C. M. Reversible Structural Transition in MIL-53 with Large Temperature Hysteresis. *J. Am. Chem. Soc.* **2008**, *130*, 11813−11818.

(17) Ai, L.; Zhang, C.; Li, L.; Jiang, J. Iron Terephthalate Metal−Organic Framework: Revealing the Effective Activation of Hydrogen Peroxide for the Degradation of Organic Dye under Visible Light Irradiation. *Appl. Catal. B: Environ.* **2014**, 191−200.

(18) Liang, R.; Jing, F.; Shen, L.; Qin, N.; Wu, L. MIL-53(Fe) as a Highly Efficient Bifunctional Photocatalyst for the Simultaneous Reduction of Cr(VI) and Oxidation of Dyes. *J. Hazard. Mater.* **2015**, *287*, 364−372.

(19) Zhang, C. F.; Qiu, L. G.; Ke, F.; Zhu, Y. J.; Yuan, Y. P.; Xu, G. S.; Jiang, X. A Novel Magnetic Recyclable Photocatalyst Based on a Core−Shell Metal−Organic Framework Fe_3O_4@MIL-100(Fe) for The Decolorization of Methylene Blue Dye. *J. Mater. Chem. A* **2013**, *1*, 14329−14334.

(20) Wang, C.; deKrafft, K. E.; Lin, W. Pt Nanoparticles@ Photoactive Metal−Organic Frameworks: Efficient Hydrogen Evolution via Synergistic Photoexcitation and Electron Injection. *J. Am. Chem. Soc.* **2012**, *134*, 7211−7214.

(21) Zhang, Y.; Li, G.; Lu, H.; Lv, Q.; Sun, Z. Synthesis, Characterization and Photocatalytic Properties of MIL-53(Fe)-Graphene Hybrid Materials. *RSC Adv.* **2014**, *4*, 7594−7600.

(22) Liu, X.; Zhou, H.; Zhang, Y.; Liu, Y.; Yuan, A. Syntheses, Characterizations, and Adsorption Properties of MIL-101/Graphene Oxide Composites. *Chin. J. Chem.* **2012**, *30*, 2563−2566.

(23) Yang, X.; Tu, Y.; Li, L.; Shang, S.; Tao, X. Well-Dispersed Chitosan/Graphene Oxide Nanocomposites. *ACS Appl. Mater. Interfaces* **2010**, *2*, 1707−1713.

(24) Zhang, H. B.; Yan, Q.; Zheng, W. G.; He, Z.; Yu, Z. Z. Tough Graphene−Polymer Microcellular Foams for Electromagnetic Interference Shielding. *ACS Appl. Mater. Interfaces* **2011**, *3*, 918−924.

(25) Cheng, G.; Akhtar, M. S.; Yang, O. B.; Stadler, F. J. Novel Preparation of Anatase TiO_2@Reduced Graphene Oxide Hybrids for High-Performance Dye-Sensitized Solar Cells. *ACS Appl. Mater. Interfaces* **2013**, *5*, 6635−6642.

(26) Xian, J.; Li, D.; Chen, J.; Li, X.; He, M.; Shao, Y.; Yu, L.; Fang, J. TiO_2 Nanotube Array-Graphene-CdS Quantum Dots Composite Film in Z-Scheme with Enhanced Photoactivity and Photostability. *ACS Appl. Mater. Interfaces* **2014**, *6*, 13157−13166.

(27) Mann, S. Self-Assembly and Transformation of Hybrid Nano-Objects and Nanostructures under Equilibrium and Non-Equilibrium Conditions. *Nat. Mater.* **2009**, *8*, 781−792.

(28) Wang, Y.; Wang, W.; Mao, H.; Lu, Y.; Lu, J.; Huang, J.; Ye, Z.; Lu, B. Electrostatic Self-Assembly of $BiVO_4$-Reduced Graphene Oxide

DOI: 10.1021/acsami.5b00682
ACS Appl. Mater. Interfaces 2015, 7, 9507−9515

Nanocomposites for Highly Efficient Visible Light Photocatalytic Activities. *ACS Appl. Mater. Interfaces* **2014**, *6*, 12698−12706.
(29) Chen, Z.; Zhang, N.; Xu, Y. J. Synthesis of Graphene−ZnO Nanorod Nanocomposites with Improved Photoactivity and Anti-Photocorrosion. *CrystEngComm* **2013**, *15*, 3022−3030.
(30) Chung, K.; Rani, A.; Lee, J.-E.; Kim, J. E.; Kim, Y.; Yang, H.; Kim, S. O.; Kim, D.; Kim, D. H. Systematic Study on the Sensitivity Enhancement in Graphene Plasmonic Sensors Based on Layer-by-Layer Self-Assembled Graphene Oxide Multilayers and Their Reduced Analogues. *ACS Appl. Mater. Interfaces* **2015**, *7*, 144−151.
(31) Horcajada, P.; Serre, C.; Maurin, G.; Ramsahye, N. A.; Balas, F.; Vallet-Regí, M. a.; Sebban, M.; Taulelle, F.; Férey, G. r. Flexible Porous Metal−Organic Frameworks for a Controlled Drug Delivery. *J. Am. Chem. Soc.* **2008**, *130*, 6774−6780.
(32) Llewellyn, P. L.; Horcajada, P.; Maurin, G.; Devic, T.; Rosenbach, N.; Bourrelly, S.; Serre, C.; Vincent, D.; Loera-Serna, S.; Filinchuk, Y.; Férey, G. Complex Adsorption of Short Linear Alkanes in the Flexible Metal−Organic Framework MIL-53(Fe). *J. Am. Chem. Soc.* **2009**, *131* (36), 13002−13008.
(33) Shen, L.; Huang, L.; Liang, S.; Liang, R.; Qin, N.; Wu, L. Electrostatically Derived Self-Assembly of NH_2-Mediated Zirconium MOFs with Graphene for Photocatalytic Reduction of Cr(VI). *RSC Adv.* **2014**, *4*, 2546−2549.
(34) Idris, A.; Hassan, N.; Rashid, R.; Ngomsik, A.-F. Kinetic and Regeneration Studies of Photocatalytic Magnetic Separable Beads for Chromium (VI) Reduction Under Sunlight. *J. Hazard. Mater.* **2011**, *186*, 629−635.
(35) Li, D.; Muller, M. B.; Gilje, S.; Kaner, R. B.; Wallace, G. G. Processable Aqueous Dispersions of Graphene Nanosheets. *Nat. Nano* **2008**, *3*, 101−105.
(36) Szabó, T.; Tombácz, E.; Illés, E.; Dékány, I. Enhanced Acidity and pH-Dependent Surface Charge Characterization of Successively Oxidized Graphite Oxides. *Carbon* **2006**, *44*, 537−545.
(37) Lin, R.; Shen, L.; Ren, Z.; Wu, W.; Tan, Y.; Fu, H.; Zhang, J.; Wu, L. Enhanced Photocatalytic Hydrogen Production Activity via Dual Modification of MOF and Reduced Graphene Oxide on CdS. *Chem. Commun.* **2014**, *50*, 8533−8535.
(38) Liang, Y. T.; Vijayan, B. K.; Gray, K. A.; Hersam, M. C. Minimizing Graphene Defects Enhances Titania Nanocomposite-Based Photocatalytic Reduction of CO_2 for Improved Solar Fuel Production. *Nano Lett.* **2011**, *11*, 2865−2870.
(39) Yang, M.-Q.; Xu, Y.-J. Basic Principles for Observing the Photosensitizer Role of Graphene in the Graphene−Semiconductor Composite Photocatalyst from a Case Study on Graphene−ZnO. *J. Phys. Chem. C* **2013**, *117*, 21724−21734.
(40) Bordiga, S.; Lamberti, C.; Ricchiardi, G.; Regli, L.; Bonino, F.; Damin, A.; Lillerud, K. P.; Bjorgen, M.; Zecchina, A. Electronic and Vibrational Properties of a MOF-5 Metal−Organic Framework: ZnO Quantum Dot Behaviour. *Chem. Commun.* **2004**, 2300−2301.
(41) Vuong, G. T.; Pham, M. H.; Do, T. O. Direct Synthesis and Mechanism of the Formation of Mixed Metal Fe_2Ni-MIL-88B. *CrystEngComm* **2013**, *15*, 9694−9703.
(42) Vuong, G. T.; Pham, M. H.; Do, T. O. Synthesis and Engineering Porosity of a Mixed Metal Fe_2Ni−MIL 88B Metal−Organic Framework. *Dalton Trans.* **2013**, *42*, 550−557.
(43) Yang, M. Q.; Zhang, N.; Xu, Y. J. Synthesis of Fullerene−, Carbon Nanotube−, and Graphene−TiO_2 Nanocomposite Photocatalysts for Selective Oxidation: a Comparative Study. *ACS Appl. Mater. Interfaces* **2013**, *5*, 1156−1164.
(44) Zhang, Y.; Zhang, N.; Tang, Z. R.; Xu, Y. J. Improving the Photocatalytic Performance of Graphene−TiO_2 Nanocomposites via a Combined Strategy of Decreasing Defects of Graphene and Increasing Interfacial Contact. *Phys. Chem. Chem. Phys.* **2012**, *14*, 9167−9175.
(45) Ye, L.; Fu, J.; Xu, Z.; Yuan, R.; Li, Z. Facile One-Pot Solvothermal Method to Synthesize Sheet-on-Sheet Reduced Graphene Oxide (RGO)/$ZnIn_2S_4$ Nanocomposites with Superior Photocatalytic Performance. *ACS Appl. Mater. Interfaces* **2014**, *6*, 3483−3490.
(46) Chen, Z.; Liu, S.; Yang, M. Q.; Xu, Y. J. Synthesis of Uniform CdS Nanospheres/Graphene Hybrid Nanocomposites and Their Application as Visible Light Photocatalyst for Selective Reduction of Nitro Organics in Water. *ACS Appl. Mater. Interfaces* **2013**, *5*, 4309−4319.
(47) Zhang, N.; Zhang, Y.; Pan, X.; Fu, X.; Liu, S.; Xu, Y. J. Assembly of CdS Nanoparticles on the Two-Dimensional Graphene Scaffold as Visible-Light-Driven Photocatalyst for Selective Organic Transformation under Ambient Conditions. *J. Phys. Chem. C* **2011**, *115*, 23501−23511.
(48) Liu, S.; Chen, Z.; Zhang, N.; Tang, Z.-R.; Xu, Y.-J. An Efficient Self-Assembly of CdS Nanowires−Reduced Graphene Oxide Nanocomposites for Selective Reduction of Nitro Organics under Visible Light Irradiation. *J. Phys. Chem. C* **2013**, *117*, 8251−8261.
(49) Zhang, Y.; Tang, Z. R.; Fu, X.; Xu, Y.-J. Engineering the Unique 2D Mat of Graphene to Achieve Graphene−TiO_2 Nanocomposite for Photocatalytic Selective Transformation: What Advantage does Graphene Have over Its Forebear Carbon Nanotube? *ACS Nano* **2011**, *5*, 7426−7435.
(50) Allendorf, M. D.; Bauer, C. A.; Bhakta, R. K.; Houk, R. J. Luminescent Metal−Organic Frameworks. *Chem. Soc. Rev.* **2009**, *38*, 1330−1352.
(51) Spagnol, V.; Sutter, E.; Debiemme-Chouvy, C.; Cachet, H.; Baroux, B. EIS Study of Photo-Induced Modifications of Nano-Columnar TiO_2 Films. *Electrochim. Acta* **2009**, *54*, 1228−1232.
(52) Ishikawa, A.; Takata, T.; Kondo, J. N.; Hara, M.; Kobayashi, H.; Domen, K. Oxysulfide $Sm_2Ti_2S_2O_5$ as a Stable Photocatalyst for Water Oxidation and Reduction under Visible Light Irradiation ($\lambda \leq 650$ nm). *J. Am. Chem. Soc.* **2002**, *124*, 13547−13553.
(53) Wang, X.; Pehkonen, S. O.; Ray, A. K. Removal of Aqueous Cr(VI) by a Combination of Photocatalytic Reduction and Coprecipitation. *Ind. Eng. Chem. Res.* **2004**, *43*, 1665−1672.
(54) Yan, S. C.; Li, Z. S.; Zou, Z. G. Photodegradation of Rhodamine B and Methyl Orange over Boron-Doped g-C_3N_4 under Visible Light Irradiation. *Langmuir* **2010**, *26*, 3894−3901.
(55) Liang, S.; Liang, R.; Wen, L.; Yuan, R.; Wu, L.; Fu, X. Molecular Recognitive Photocatalytic Degradation of Various Cationic Pollutants by the Selective Adsorption on Visible-Light-Driven $SnNb_2O_6$ Nanosheet Photocatalyst. *Appl. Catal. B* **2012**, *125*, 103−110.
(56) Wan, Q.; Wang, X.; Wang, X.; Yang, N. Poly(Malachite Green) Film: Electrosynthesis, Characterization, and Sensor Application. *Polymer* **2006**, *47*, 7684−7692.

DOI: 10.1021/acsami.5b00682
ACS Appl. Mater. Interfaces 2015, 7, 9507−9515